



# Fabrication of visible-light active $\text{Fe}_2\text{O}_3$ -GQDs/NF-TiO<sub>2</sub> composite film with highly enhanced photoelectrocatalytic performance

Qi Wang <sup>a,b</sup>, Naxin Zhu <sup>a,c</sup>, Enqin Liu <sup>a</sup>, Chenlu Zhang <sup>a</sup>, John C. Crittenden <sup>b</sup>, Yi Zhang <sup>a</sup>, Yanqing Cong <sup>a,\*</sup>

<sup>a</sup> School of Environmental Science and Engineering, Zhejiang Gongshang University, Hangzhou 310018, China

<sup>b</sup> The Brook Byer Institute for Sustainable Systems and School of Civil and Environmental Engineering, Georgia Institute of Technology, Atlanta 30332, USA

<sup>c</sup> Laboratory for Advanced Materials, Research Institute of Industrial Catalysis, East China University of Science and Technology, Shanghai 200237, China



## ARTICLE INFO

### Article history:

Received 25 August 2016

Received in revised form 26 October 2016

Accepted 22 November 2016

Available online 22 November 2016

### Keywords:

Cr(VI) reduction

NF-TiO<sub>2</sub>

$\alpha$ -Fe<sub>2</sub>O<sub>3</sub>

GQDs

Photoelectrocatalytic

## ABSTRACT

Visible-light active  $\text{Fe}_2\text{O}_3$ -GQDs/NF-TiO<sub>2</sub> composite films were fabricated via sequential electro-deposition and electro-oxidation processes. The prepared photocatalytic films were extensively characterized using scanning electron microscopy (SEM), high-resolution transmission electron microscopy (HRTEM), X-ray diffraction (XRD), Raman spectroscopy and X-ray photoelectron spectroscopy (XPS). The results revealed that graphene quantum dots (GQDs) and  $\alpha$ -Fe<sub>2</sub>O<sub>3</sub> particles were simultaneously deposited onto the surface of N and F co-doped TiO<sub>2</sub> (NF-TiO<sub>2</sub>) simply using a graphite sheet instead of a Pt sheet as anode in the electro-deposition process. The NF-TiO<sub>2</sub> substrate obtained by calcining TiO<sub>2</sub> nanotubes (TiO<sub>2</sub>-NTs) in the presence of NH<sub>4</sub>F displayed pyramid shapes with dominant (101) facets. Linear sweep voltammetry (LSV), electrochemical impedance spectroscopy (EIS) and Mott-Schottky (M-S) plots indicated that the generation, separation and transfer of photogenerated charges were greatly enhanced on the novel composite. The photocurrent density of  $\text{Fe}_2\text{O}_3$ -GQDs/NF-TiO<sub>2</sub> was 4.2 times that on Fe<sub>2</sub>O<sub>3</sub>/TiO<sub>2</sub>-NTs at 0.5 V vs. Ag/AgCl under visible light irradiation. For the photoelectrocatalytic (PEC) reduction of Cr(VI) using  $\text{Fe}_2\text{O}_3$ -GQDs/NF-TiO<sub>2</sub> as photoanode with a Ti sheet as cathode, substantially enhanced activity was achieved due to the combined effect of visible-light-active components ( $\alpha$ -Fe<sub>2</sub>O<sub>3</sub> and NF-TiO<sub>2</sub>) and excellent electron mediator (GQDs). The calculated reduction rate constant was 7 times that obtained on Fe<sub>2</sub>O<sub>3</sub>/TiO<sub>2</sub>-NTs film. Furthermore, both the long-time photocurrent and cyclic PEC reduction of Cr(VI) indicated good stability of the composite film.

© 2016 Elsevier B.V. All rights reserved.

## 1. Introduction

In recent decades, semiconductor photocatalysis has been recognized as one of the most promising methods for environmental remediation [1,2]. Based on photocatalysis, an improved performance was observed in the photoelectrocatalytic (PEC) process after the introduction of bias voltage, which promoted the separation of photogenerated electron–hole pairs [3–8]. In addition, the immobilized photocatalytic films in the PEC process can be easily reused, which is critical for future practical applications. However, it is still a great challenge to develop highly efficient photocatalytic material that can utilize more solar energy.

As the most extensively studied photocatalyst, pure TiO<sub>2</sub> can absorb only UV light and cannot be directly excited by visible light, which accounts for up to approximately 43% of solar radiation. Lattice doping and surface modification have both been investigated to overcome this problem and have proven effective [1,9–11]. Non-metal doping, such as N doping, is recognized as one of the most promising way to narrow the band gap and extend the response of TiO<sub>2</sub> into visible region [10,12]. However, the oxidative power of N-doped TiO<sub>2</sub> (N-TiO<sub>2</sub>) under visible light is relatively low due to the formation of a mixed gap composed of N 2p and O 2p above the valence band (VB). For example, the degradation of formic acid, NH<sub>3</sub> or I<sup>−</sup> barely proceeded on N-TiO<sub>2</sub> [13,14]. Previously, we observed the vital role of fluorine in tuning the band structure of N-TiO<sub>2</sub> [15]. Co-doping of F could enhance the oxidative power of N-TiO<sub>2</sub> and shift the conduction band (CB) to a more positive position [16,17].

Surface modification with another narrow band-based semiconductor is also a suitable option to improve the visible light activity of TiO<sub>2</sub> [18–20]. N-type hematite ( $\alpha$ -Fe<sub>2</sub>O<sub>3</sub>, 2.2 eV) is recognized as

\* Corresponding author.

E-mail addresses: [yqcong@hotmail.com](mailto:yqcong@hotmail.com), [yqcong@zjgsu.edu.cn](mailto:yqcong@zjgsu.edu.cn) (Y. Cong).

URL: <http://mailto:yqcong@hotmail.com> (Y. Cong).

a promising candidate due to its high visible light absorption, rich abundance and low cost [21–23]. Enhanced photocatalytic activity under visible light has been reported when coupled with TiO<sub>2</sub> or N-TiO<sub>2</sub> [24–29]. Because the CB of  $\alpha$ -Fe<sub>2</sub>O<sub>3</sub> lies below the CB of TiO<sub>2</sub> [27,28], only high-energy electrons of  $\alpha$ -Fe<sub>2</sub>O<sub>3</sub>, which constitute a small fraction of photogenerated electrons, can be transferred to the CB of TiO<sub>2</sub> [25,29]. Thus, raising the CB of  $\alpha$ -Fe<sub>2</sub>O<sub>3</sub> or lowering the CB of TiO<sub>2</sub> may be beneficial for the electron transfer process. Because the co-doping of N and F can lower the CB position of TiO<sub>2</sub> [15], the construction of a  $\alpha$ -Fe<sub>2</sub>O<sub>3</sub>/NF-TiO<sub>2</sub> composite should be a more suitable choice than  $\alpha$ -Fe<sub>2</sub>O<sub>3</sub>/N-TiO<sub>2</sub> or  $\alpha$ -Fe<sub>2</sub>O<sub>3</sub>/TiO<sub>2</sub>. Low-energy electrons on  $\alpha$ -Fe<sub>2</sub>O<sub>3</sub> can be more efficiently utilized in this composite.

Moreover, carbon materials have shown excellent promoting effect in the electron transfer process [30–34]. For example, carbon nanotube, carbon quantum dots, graphene and graphene quantum dots (GQDs) were all members of carbon family [35–38]. Recently, graphene quantum dots (GQDs) with a small size (<20 nm) have drawn considerable attention. GQDs are intriguing in terms of their ability to accept and transfer photogenerated electrons due to pronounced quantum confinement and edge effects. Thus, the performance of  $\alpha$ -Fe<sub>2</sub>O<sub>3</sub>/NF-TiO<sub>2</sub> can be further enhanced after the proper introduction of GQDs.

Herein, we report the first study and fabrication of a Fe<sub>2</sub>O<sub>3</sub>-GQDs/NF-TiO<sub>2</sub> composite film with the aim of achieving highly efficient electron generation, separation and transfer. The NF-TiO<sub>2</sub> substrate with pyramid-shape and dominant (101) facets was first prepared by calcining TiO<sub>2</sub> nanotubes (TiO<sub>2</sub>-NTs) with the assistance of NH<sub>4</sub>F. The most stable (101) facets was reported to be more reductive than the star facets of (001) [39–41], where photo-deposition of Pt and reduction of O<sub>2</sub> preferentially occurred [40,42]. Herein, (101) facets acted as highly active electron reservoirs.  $\alpha$ -Fe<sub>2</sub>O<sub>3</sub> and GQDs were deposited onto the surface of NF-TiO<sub>2</sub> via sequential electro-deposition and electro-oxidation processes (Scheme 1). GQDs can be simultaneously deposited onto the surface of  $\alpha$ -Fe<sub>2</sub>O<sub>3</sub>/NF-TiO<sub>2</sub> simply using a graphite sheet instead of a Pt sheet as anode in the electro-deposition process. The generation, separation and transfer of photogenerated charges on the prepared film electrodes were compared using linear sweep voltammetry (LSV), electrochemical impedance spectroscopy (EIS) and Mott-Schottky (M-S) plots. Moreover, Cr(VI), a carcinogen and mutagen was used as a model pollutant for capturing the cathode electrons, with coexisting organic pollutants as hole scavengers. Due to the combined effect of visible-light-active components ( $\alpha$ -Fe<sub>2</sub>O<sub>3</sub> and NF-TiO<sub>2</sub>) and the excellent electron conductors (GQDs), a highly enhanced PEC performance was demonstrated using Fe<sub>2</sub>O<sub>3</sub>-GQDs/NF-TiO<sub>2</sub> as photoanode and a Ti sheet as cathode.

## 2. Experimental

### 2.1. Preparation of the Fe<sub>2</sub>O<sub>3</sub>-GQDs/NF-TiO<sub>2</sub> film electrode

NF-TiO<sub>2</sub> film was obtained by calcining amorphous TiO<sub>2</sub>-NTs film (prepared by a traditional anodizing process [27,43]) in the presence of NH<sub>4</sub>F at 450 °C for 2 h (Scheme 1). TiO<sub>2</sub>-NTs can be simultaneously etched and doped by HF and NH<sub>3</sub> originating from NH<sub>4</sub>F decomposition. As a control experiment, N-TiO<sub>2</sub> was also prepared using NH<sub>4</sub>Cl instead of NH<sub>4</sub>F in the calcination process. The initial ratio of NH<sub>4</sub>F to Ti substrate (cm<sup>2</sup>) was maintained at an optimal value of 0.2 g/cm<sup>2</sup>.

Fe<sub>2</sub>O<sub>3</sub>-GQDs/NF-TiO<sub>2</sub> films were prepared via consecutive electro-deposition and electro-oxidation processes (Scheme 1). Fe<sub>2</sub>O<sub>3</sub>/NF-TiO<sub>2</sub> was also prepared for comparison. The two different films were fabricated using different anodes (Pt sheet or graphite) in the electro-deposition process. For the deposition of

Fe<sub>2</sub>O<sub>3</sub>, Fe<sup>3+</sup> was first adsorbed onto the surface of NF-TiO<sub>2</sub> by soaking the NF-TiO<sub>2</sub> film in Fe(NO<sub>3</sub>)<sub>3</sub> aqueous solution (0.1 M) and then converted to Fe<sup>0</sup> in the electro-deposition process. Finally, the electro-deposited Fe<sup>0</sup> was transformed to Fe<sub>2</sub>O<sub>3</sub> via anodization in a 1.0 M KOH aqueous solution for 2 min. As controls, Fe<sub>2</sub>O<sub>3</sub>/TiO<sub>2</sub>-NTs and Fe<sub>2</sub>O<sub>3</sub>/N-TiO<sub>2</sub> were also prepared in a manner similar to the Fe<sub>2</sub>O<sub>3</sub>/NF-TiO<sub>2</sub> preparation process except that TiO<sub>2</sub>NTs or N-TiO<sub>2</sub> was used as the substrate for Fe<sub>2</sub>O<sub>3</sub> loading instead of NF-TiO<sub>2</sub>.

### 2.2. Characterization

The morphology and structure of the prepared film samples were observed by a scanning electron microscope (SEM, Hitachi S-4800, Tokyo, Japan) and a high-resolution transmission electron microscope (HRTEM, JEOL JEM-2010, Tokyo, Japan). The chemical state of component elements in the film samples was investigated by a VG Thermo Escalab 220i-XL X-ray photoelectron spectroscopy (XPS) with Al K $\alpha$  at 1,486.6 eV. The binding energies of Ti 2p, O 1s, C 1s, Fe 2p, N 1s and F 1s were referenced against C 1s (284.6 eV). The crystal phases were detected by X-ray diffractometry (XRD) using a Bruke Regaku D/Max-2500. The vibration modes were detected by Raman spectra which were recorded on a thermo scientific DXR with exciting wavelength of 633 nm. The diffuse reflectance UV-vis absorption was recorded on a Hitachi U-3010 spectrophotometer. The photo-response of the prepared films was tested under chopped light irradiation (500 W Xe lamp, Shanghai lansheng) by an electrochemical station (CHI 660E). EIS analysis and M-S plots were also measured in a three-electrode configuration by a CHI 660E electrochemical station.

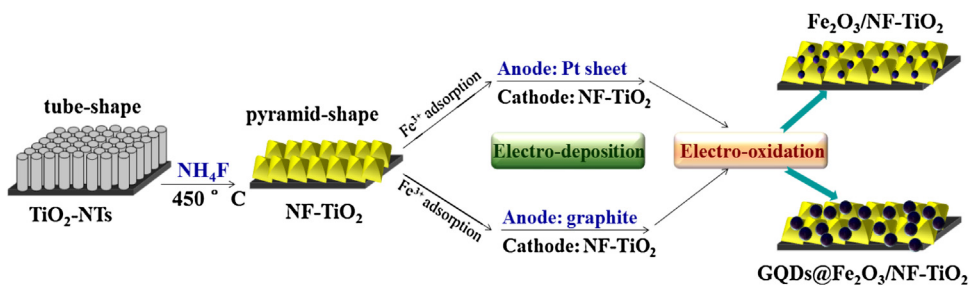
### 2.3. PEC study

Unless otherwise noted, the PEC activities of the prepared film electrodes (anode) were compared via the PEC reduction of Cr(VI) (80  $\mu$ M) with Na<sub>2</sub>SO<sub>4</sub> (0.2 mol/L) as the electrolyte and 1 mM EDTA as a hole scavenger. A constant DC potential of 2.0 V was applied to the photoanode with a Ti sheet as the cathode. The photoanode was irradiated by visible light ( $\lambda > 420$  nm, ca. 80 mW cm<sup>-2</sup>) emitted from a halogen lamp (CEL-IW500, Beijing Teach Jinyuan Technology Co., Ltd.) fitted with a cut-off filter and surrounded by a cooling water jacket. Before turning on the light, the electrode was immersed in Cr(VI) solution for 30 min to achieve adsorption-desorption equilibrium. Typically, the initial solution pH was adjusted to 3.0. The concentration of Cr(VI) at different time intervals was measured using the 1,5-diphenylcarbazide colorimetric method [44,45] on a UV-vis spectrophotometer (UV-2102PC, Unico Instruments Co., Ltd.). The purple complex of Cr(VI) 540 nm after adding chromogenic agent was barely affected by coexisting EDTA (Fig. S1). Meanwhile, pH variations as a function of PEC reaction time were also monitored (Fig. S2). In addition, the concentrations of coexisting organics, including EDTA (1.0 mM), phenol (10 mg/L), and methylene blue (MB, 10  $\mu$ M) during the PEC process were also monitored. The colorless phenol and EDTA were detected by HPLC, whereas the MB dye was monitored by its maximum absorption at 664 nm on a UV-vis spectrophotometer.

## 3. Results and discussion

### 3.1. SEM and HRTEM

The prepared film electrodes were first characterized by SEM to investigate possible morphology changes. As shown in Fig. 1a, the Fe<sub>2</sub>O<sub>3</sub>/TiO<sub>2</sub>-NTs surface was composed of TiO<sub>2</sub> nanotubes and Fe<sub>2</sub>O<sub>3</sub> particles. Pyramid-shaped NF-TiO<sub>2</sub> was observed after calcining the TiO<sub>2</sub>-NTs substrate in the presence of NH<sub>4</sub>F (Fig. 1b).



**Scheme 1.** Schematic depicting the preparation of  $\text{Fe}_2\text{O}_3/\text{NF-TiO}_2$  and  $\text{Fe}_2\text{O}_3\text{-GQDs}/\text{NF-TiO}_2$  films.

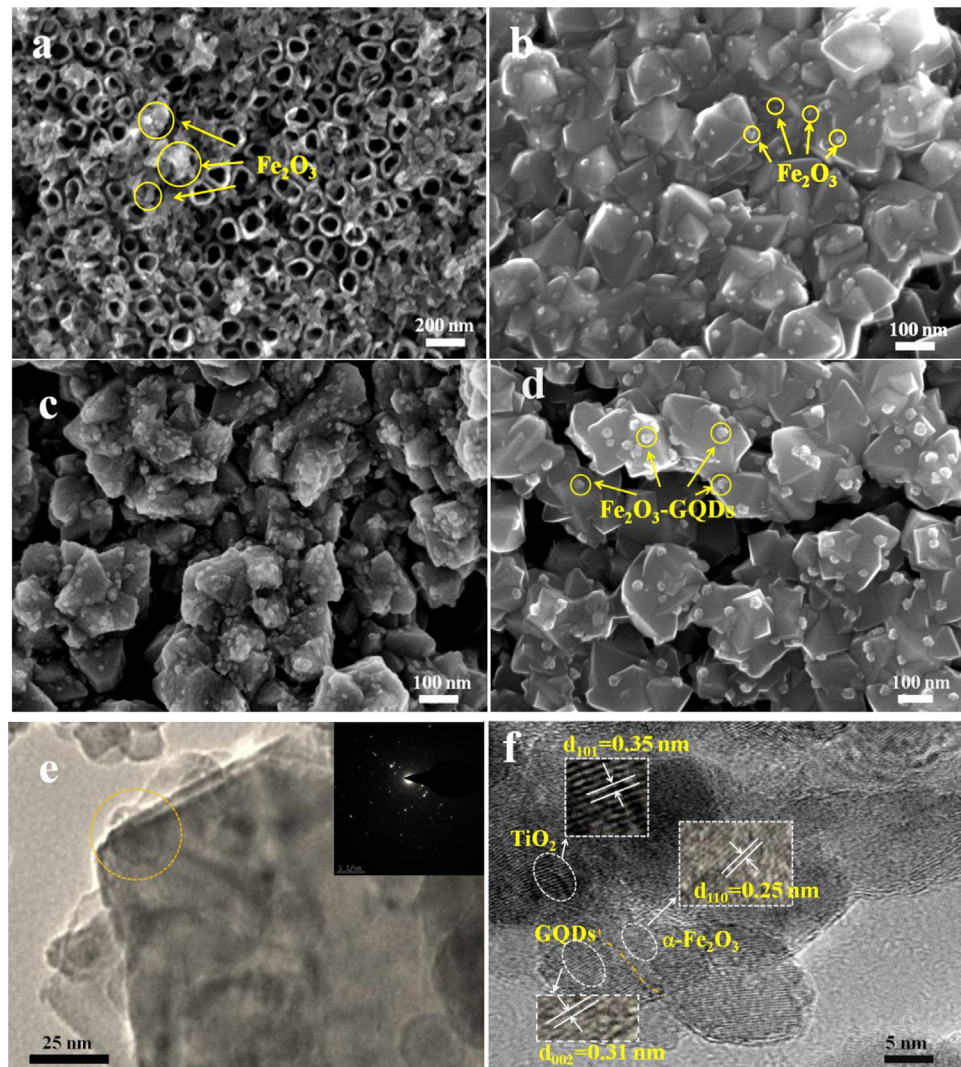


**Fig. 1.** SEM images of (a)  $\text{Fe}_2\text{O}_3/\text{TiO}_2\text{-NTs}$ , (b)  $\text{Fe}_2\text{O}_3/\text{NF-TiO}_2$ , (c)  $\text{Fe}_2\text{O}_3\text{-GQDs}/\text{NF-TiO}_2$  (intermediate state) and (d)  $\text{Fe}_2\text{O}_3\text{-GQDs}/\text{NF-TiO}_2$ ; (e) TEM and (f) HRTEM images of  $\text{Fe}_2\text{O}_3\text{-GQDs}/\text{NF-TiO}_2$ .

A control experiment using pure Ti foil instead of  $\text{TiO}_2\text{-NTs}$  was also performed to understand this interesting phenomenon. No pyramid-shaped structures were observed under identical calcination conditions (Fig. S3a). Moreover, a  $\text{TiO}_2\text{-NTs}$  surface was also calcined in the presence of  $\text{NH}_4\text{Cl}$ . The use of  $\text{NH}_4\text{Cl}$  instead of  $\text{NH}_4\text{F}$  led to the formation of particle-shaped products (Fig. S3b). In brief, the use of tubular structures as precursors and  $\text{NH}_4\text{F}$  as the additive were both essential for the formation of pyramid-shaped  $\text{NF-TiO}_2$ .

For  $\text{Fe}_2\text{O}_3/\text{NF-TiO}_2$ , smaller  $\text{Fe}_2\text{O}_3$  particles (10–15 nm) were more uniformly deposited and dispersed on the surface of  $\text{NF-TiO}_2$

(Fig. 1b). Interestingly, using different anodes (Pt sheet or a graphite sheet) during the electro-deposition process will lead to the formation of different  $\text{Fe}_2\text{O}_3$ -loaded electrodes ( $\text{Fe}_2\text{O}_3/\text{NF-TiO}_2$  and  $\text{Fe}_2\text{O}_3\text{-GQDs}/\text{NF-TiO}_2$ ). For example, as shown in Scheme 1, when a graphite sheet is used as the anode for the electro-deposition of Fe nanoparticles, graphite will be exfoliated simultaneously (Fig. S4) and will cover the surface of  $\text{NF-TiO}_2$ . As shown in Fig. 1c, the intermediate state was captured when the next oxidation step was not performed. The surface of  $\text{NF-TiO}_2$  and deposited  $\text{Fe}^0$  nanoparticles was clearly covered by graphite-originated material. When

this intermediate state was further electrochemically oxidized in 1.0 mol/L KOH aqueous solution, Fe<sup>0</sup> was converted to Fe<sub>2</sub>O<sub>3</sub> and the graphite-originated cover disappeared, leaving a clean NF-TiO<sub>2</sub> surface. However, the particle size loaded onto NF-TiO<sub>2</sub> (Fig. 1d) was observed to be considerably larger than that on Fe<sub>2</sub>O<sub>3</sub>/NF-TiO<sub>2</sub> using Pt as anode in the electro-deposition process. High-resolution TEM (HRTEM) was performed to obtain more detailed structural information. Fig. 1e illustrates that particles with a diameter of approximately 18 nm were loaded on the pyramid-shaped substrate. The HRTEM image of the selected area is presented in Fig. 1f. After fast Fourier transform (FFT), the lattice fringes of TiO<sub>2</sub>, α-Fe<sub>2</sub>O<sub>3</sub> and GQDs can all be identified. For example, the lattice fringe spacing of 0.31 nm corresponds to the lattice fringes of (002) planes of GQDs [46,47], whereas the values of 0.25 and 0.35 nm were ascribed to the (110) plane of α-Fe<sub>2</sub>O<sub>3</sub> [48] and the (101) plane of anatase TiO<sub>2</sub>, respectively.

### 3.2. XRD and raman spectra

XRD patterns of the prepared film electrodes were investigated, and the results are shown in Fig. 2A. The diffraction peaks at 25.3°, 37.9°, 48.1°, 54.0°, 55.1°, 68.8°, 70.3° and 75.1° correspond to (101), (004), (200), (105), (211), (116), (220) and (215) planes of anatase TiO<sub>2</sub>, respectively. Distinct Rutile (110) signal can be observed in NF-TiO<sub>2</sub> (curve a). The presence of a small fraction of rutile may be beneficial for electron–hole separation under irradiation due to the formation of heterojunction. As for Fe<sub>2</sub>O<sub>3</sub>/TiO<sub>2</sub>-NTs (curve b), pure anatase TiO<sub>2</sub> and distinct signals of the Ti substrate were observed. The characteristic diffraction peaks corresponding to α-Fe<sub>2</sub>O<sub>3</sub> (JCPDS No. 33-0664) can also be observed [22]. However, very weak α-Fe<sub>2</sub>O<sub>3</sub> signals can be observed in either Fe<sub>2</sub>O<sub>3</sub>/NF-TiO<sub>2</sub> or Fe<sub>2</sub>O<sub>3</sub>-GQDs/NF-TiO<sub>2</sub>, which is probably due to the relatively small amount. Furthermore, Raman spectrum was carried out to confirm the presence of Fe<sub>2</sub>O<sub>3</sub>. As shown in Fig. 2B, typical A<sub>1g</sub> and E<sub>1g</sub> Raman modes of α-Fe<sub>2</sub>O<sub>3</sub> [26] can be observed in both Fe<sub>2</sub>O<sub>3</sub>/NF-TiO<sub>2</sub> and Fe<sub>2</sub>O<sub>3</sub>-GQDs/NF-TiO<sub>2</sub>.

Compared to Fe<sub>2</sub>O<sub>3</sub>/NF-TiO<sub>2</sub>, a weak signal at 26.4° can be observed on Fe<sub>2</sub>O<sub>3</sub>-GQDs/NF-TiO<sub>2</sub> (Fig. S5), which is different from the characteristic and sharp diffraction peaks of either raw graphite (26.5°) [49] or expanded graphite (26.6°) [50]. Recently, Parvez et al. reported the electrochemical exfoliation of graphite into a graphene sheet, where the exfoliated products displayed a characteristic XRD peak at 26.3° [51]. The electrodeposition process (Scheme 1) in the present study is highly similar to Parvez's procedure, where graphite and Na<sub>2</sub>SO<sub>4</sub> (which exhibited a pronounced exfoliation efficiency) were used as the anode and electrolyte, respectively. In addition to electro-deposition, subsequent electro-oxidation was added in the present study, which may destroy the sheet structure of graphene, leading to the small particle-shaped GQDs. The sp<sup>2</sup> configuration of GQDs was further verified by Raman spectrum. As shown in Fig. 2B, distinct peaks of the D band (1345 cm<sup>-1</sup>) and G band (1603 cm<sup>-1</sup>) of graphene [52] can be observed on Fe<sub>2</sub>O<sub>3</sub>-GQDs/NF-TiO<sub>2</sub>, whereas no such peaks appeared on Fe<sub>2</sub>O<sub>3</sub>/NF-TiO<sub>2</sub>. These results illustrate that GQDs were simultaneously formed and deposited together with Fe<sub>2</sub>O<sub>3</sub> onto the surface of NF-TiO<sub>2</sub>.

### 3.3. XPS

The chemical composition of Fe<sub>2</sub>O<sub>3</sub>-GQDs/NF-TiO<sub>2</sub> was further revealed by XPS spectra. As shown in Fig. 3A, signals of Ti 2p, O 1s, C 1s, Fe 2p, N 1s and F 1s can be observed. The N 1s and F 1s spectra, displayed in the insert of Fig. 3A, indicated the presence of O-Ti-N [53] and Ti-F species [54]. The high-resolution spectrum of C 1s (Fig. 3B) revealed the presence of C=C (284.4 eV), C-C (284.8 eV), C-O (285.4 eV) and O-C=O (288.2 eV) species [55]. As for Fe 2p

(Fig. 3C), the two peaks at 711.2 eV and 724.8 eV were ascribed to Fe 2p<sub>1/2</sub> and Fe 2p<sub>3/2</sub>, respectively. The distance between Fe 2p<sub>1/2</sub> and Fe 2p<sub>3/2</sub> is 13.6 eV, corresponding to Fe<sup>3+</sup> in α-Fe<sub>2</sub>O<sub>3</sub> [56,57]. An approximately 0.8 eV positive shift in the binding energy of Fe 2p can be observed in Fe<sub>2</sub>O<sub>3</sub>-GQDs/NF-TiO<sub>2</sub> relative to that in Fe<sub>2</sub>O<sub>3</sub>/NF-TiO<sub>2</sub>. However, a negligible shift was observed for Ti 2p (Fig. 3D). Therefore, the presence of GQDs appears to play a vital role in affecting the electronic environment around the Fe atoms. Because it has been verified by HRTEM (Fig. 1d) that the GQDs and Fe<sub>2</sub>O<sub>3</sub> nanoparticles were in contact with each other, the sp<sup>2</sup> configuration of C=C bonds in GQDs will aid in the dispersion of electron density from Fe atoms to GQDs. Thus, the electron density around Fe<sub>2</sub>O<sub>3</sub> will decrease, resulting in a higher binding energy [58]. In summary, it is reasonable to speculate that the electronic state of Fe<sub>2</sub>O<sub>3</sub> is considerably different due to being covered by GQDs, which leads to the formation of Fe<sub>2</sub>O<sub>3</sub>-GQDs loaded onto pyramid-shaped NF-TiO<sub>2</sub>.

### 3.4. Electrochemical characterizations

The photocurrent response of the prepared films was tested and compared in 0.1 M Na<sub>2</sub>SO<sub>4</sub> and Na<sub>2</sub>SO<sub>3</sub> mixed aqueous solution under both chopped visible light ( $\lambda > 420$  nm) and UV-vis light irradiation. As illustrated in Fig. 4, the Fe<sub>2</sub>O<sub>3</sub>-GQDs/NF-TiO<sub>2</sub> film exhibited the highest current density. Interestingly, large dark currents were always observed on NF-TiO<sub>2</sub> based samples. For more accurate comparison of the photocurrent density among different photoanodes, the dark currents were deducted and the results were shown in Fig. S6. Under visible light irradiation (Fig. S6A), the photocurrent density was  $-0.252 \text{ mA/cm}^{-2}$  at 0.5 V vs. Ag/AgCl on Fe<sub>2</sub>O<sub>3</sub>-GQDs/NF-TiO<sub>2</sub>, which was approximately 4.2 times that of Fe<sub>2</sub>O<sub>3</sub>/TiO<sub>2</sub>-NTs ( $-0.059 \text{ mA/cm}^{-2}$ ). Compared to pristine TiO<sub>2</sub>-NTs, which cannot be excited by visible light, a greatly enhanced current density was also observed on Fe<sub>2</sub>O<sub>3</sub>/TiO<sub>2</sub>-NTs (Fig. S7), indicating that Fe<sub>2</sub>O<sub>3</sub> acts as a visible light sensitizer. In addition, although the Fe<sub>2</sub>O<sub>3</sub>/NF-TiO<sub>2</sub> film (Fig. 4A, curve c) was prepared by a similar process as the Fe<sub>2</sub>O<sub>3</sub>-GQDs/NF-TiO<sub>2</sub> film, a greatly enhanced photocurrent response was observed on the latter one. The difference was ascribed to the introduction of GQDs, which may be beneficial for electron transfer. Moreover, the onset potential of different photoanodes were also compared (Fig. S8) [59,60]. It showed that more negative onset potential and increased photocurrent density can be observed on Fe<sub>2</sub>O<sub>3</sub>-GQDs/NF-TiO<sub>2</sub> film electrode.

EIS measurements were performed as EIS Nyquist plots can provide useful information on the electron-transfer process across the electrode-electrolyte interface. The EIS Nyquist plots of the different film electrodes were compared and the results were presented in Fig. S9. It can be observed that Fe<sub>2</sub>O<sub>3</sub>-GQDs/NF-TiO<sub>2</sub> exhibited smallest circular radius both in the dark and under visible light irradiation. Since small circular radius typically indicates a lower charge transfer resistance [61], lowest charge transfer resistance can be deduced on Fe<sub>2</sub>O<sub>3</sub>-GQDs/NF-TiO<sub>2</sub>. In order to clarify the role of GQDs, The EIS Nyquist plots of Fe<sub>2</sub>O<sub>3</sub>/NF-TiO<sub>2</sub> and Fe<sub>2</sub>O<sub>3</sub>-GQDs/NF-TiO<sub>2</sub> were also compared. As shown in Fig. 5A, the introducing of GQDs can greatly reduce charge transfer resistance.

In addition to EIS analysis, M-S plots under dark conditions were also investigated to compare the charge carrier density of different film electrodes. The carrier density can be deduced from the slopes of the M-S plots using the following equation [62]:

$$C_{SC}^{-2} = \frac{2}{\varepsilon_0 ee N_D} (E - E_{fb} - \frac{kT}{e}) \quad (1)$$

where  $C_{SC}$  is the space-charge layer capacitance,  $N_D$  is the dopant density,  $\varepsilon_0$  is the vacuum permittivity,  $\varepsilon$  is the relative dielectric constant of the oxide film,  $k$  is the Boltzmann constant,  $T$  is the

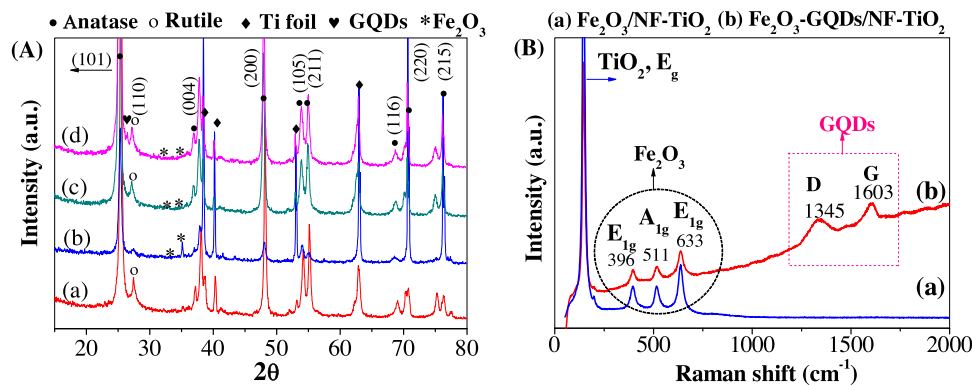


**Fig. 2.** (A) XRD patterns of NF-TiO<sub>2</sub> (a), Fe<sub>2</sub>O<sub>3</sub>/TiO<sub>2</sub>-NTs (b), Fe<sub>2</sub>O<sub>3</sub>/NF-TiO<sub>2</sub> (c) and Fe<sub>2</sub>O<sub>3</sub>-GQDs/NF-TiO<sub>2</sub> (d); (B) Raman spectra of Fe<sub>2</sub>O<sub>3</sub>/NF-TiO<sub>2</sub> (a) and Fe<sub>2</sub>O<sub>3</sub>-GQDs/NF-TiO<sub>2</sub> (b).

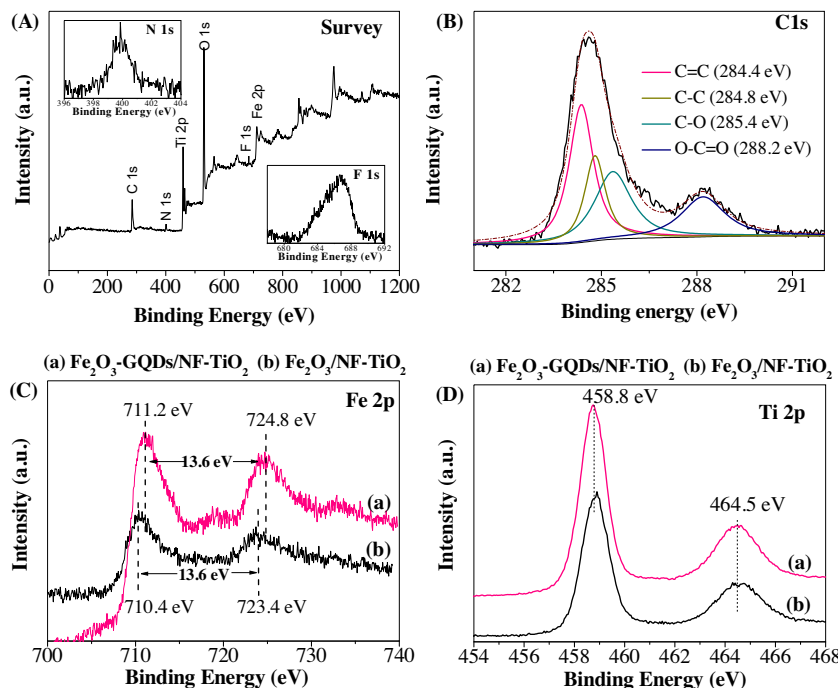


**Fig. 3.** (A) XPS survey spectrum taken from the surface of Fe<sub>2</sub>O<sub>3</sub>-GQDs/NF-TiO<sub>2</sub>, insert: XPS spectra of N 1s and F 1s; (B) High-resolution XPS spectra of C 1s region; (C) Fe 2p and (D) Ti 2p region for Fe<sub>2</sub>O<sub>3</sub>-GQDs/NF-TiO<sub>2</sub> and Fe<sub>2</sub>O<sub>3</sub>/NF-TiO<sub>2</sub>.

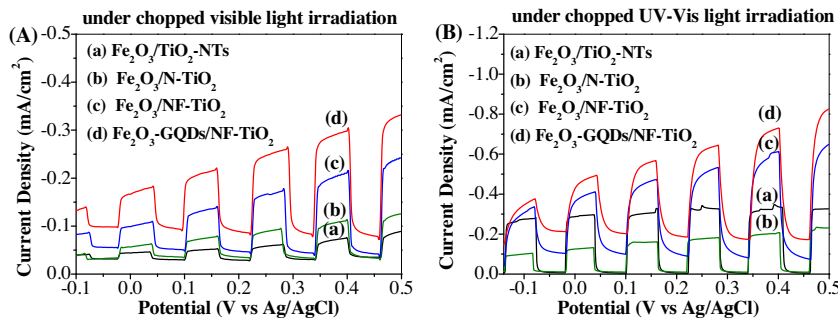


**Fig. 4.** Photocurrent response of different films under the irradiation of (A) chopped visible light ( $\lambda > 420$  nm) and (B) chopped UV-vis light.

temperature and  $kT/e$  is a negligibly small correction term. As illustrated in Fig. 5B, the slope observed on Fe<sub>2</sub>O<sub>3</sub>-GQDs/NF-TiO<sub>2</sub> was much smaller after the introducing of GQDs, indicating higher carrier density. Thus, Fe<sub>2</sub>O<sub>3</sub>-GQDs/NF-TiO<sub>2</sub> is highly likely to achieve a better PEC performance when it is used for the removal of pol-

lutants due to the easier generation and transfer of electron-hole pairs.

Overall, easier generation, more efficient separation and enhanced transfer efficiency of photogenerated electron-hole pairs can be achieved on an Fe<sub>2</sub>O<sub>3</sub>-GQDs/NF-TiO<sub>2</sub> due to the combined

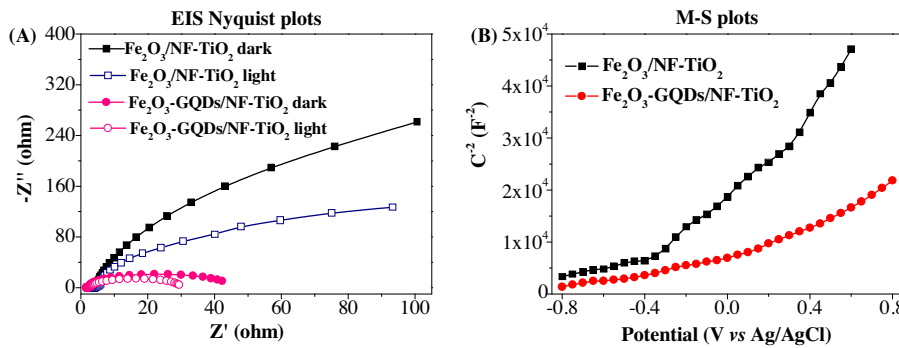


**Fig. 5.** (A) EIS Nyquist plots measured in 0.5 M  $\text{Na}_2\text{SO}_4$  aqueous solution with a frequency range of 100 kHz–0.01 Hz and a scan rate of  $5 \text{ mV s}^{-1}$ ; (B) M-S plots of different film electrodes measured in 0.2 M  $\text{Na}_2\text{SO}_4$  at 500 Hz.

effect of the visible-light-active components ( $\text{Fe}_2\text{O}_3$  and NF-TiO<sub>2</sub>) and the excellent electron mediator (GQDs). Therefore, the utilization of the superior photoelectrochemical properties for PEC applications in environmental remediation should be further investigated.

### 3.5. PEC activity

Hexavalent chromium (Cr(VI)) is toxic, carcinogenic and highly mobile in water and soil. Every year, a tremendous amount of wastewater containing Cr(VI) is discharged from industrial processes, such as electroplating, leather tanning, wood preservation and pigment use [15,44]. Thus, the detoxification of Cr(VI) is of vital importance. Cr(VI) is typically reduced to nontoxic Cr(III), which can be removed from aqueous solutions in the form of Cr(OH)<sub>3</sub>. Compared to traditional processes for Cr(VI) reduction, photocatalytic and PEC methods are efficient and environmentally friendly, which can avoid secondary pollution [63].

In the present study, Cr(VI) was selected as a model pollutant. The prepared film samples were tested as photoanode with a Ti sheet as cathode for the reduction of Cr(VI) under visible light. As shown in Fig. 6A,  $\text{Fe}_2\text{O}_3\text{-GQDs}/\text{NF-TiO}_2$  exhibited the highest PEC activity among the tested photoanodes. The estimated rate constant ( $k$ : 0.0231 min<sup>-1</sup>) (Fig. 6B) was 7 times that of  $\text{Fe}_2\text{O}_3/\text{TiO}_2\text{-NTs}$  ( $k$ : 0.0033 min<sup>-1</sup>). Since GQDs were reported to enhance the PEC activity of TiO<sub>2</sub> [35,36], control experiment using GQDs/NF-TiO<sub>2</sub> as photoanode was also carried out in the present study. As shown in Fig. 6B, about 4 times rate constant enhancement can still be observed on  $\text{Fe}_2\text{O}_3\text{-GQDs}/\text{NF-TiO}_2$  relative to GQDs/NF-TiO<sub>2</sub> ( $k$ : 0.0062 min<sup>-1</sup>). Thus, the co-loading of  $\text{Fe}_2\text{O}_3$  and GQDs are very important. Besides, pH of the solutions before, during and after photocatalytic reaction were also measured and the results were presented in Fig. S2. It can be observed that pH of the solutions gradually increased from 3.0 to 3.5.

The optimal  $\text{Fe}_2\text{O}_3\text{-GQDs}/\text{NF-TiO}_2$  film was further tested in single photocatalytic (PC) or electrocatalytic (EC) processes to confirm the superiority of the PEC process. As shown in Figs. 6C–D, a synergistic effect can be observed in the PEC process, and the synergistic factor (SF) was calculated to be 2.9 according to the following equation [64]:

$$SF = \frac{k_{\text{PEC}}}{k_{\text{PEC}} + k_{\text{EC}}} \quad (2)$$

where  $k_{\text{PEC}}$ ,  $k_{\text{PC}}$  and  $k_{\text{EC}}$  represent rate constants for Cr(VI) reduction in the PEC, PC and EC processes, respectively.

Because the photocatalytic performance of  $\text{Fe}_2\text{O}_3\text{-GQDs}/\text{NF-TiO}_2$  can be markedly increased with the assistance of applied potential, the effect of different applied potentials was investigated, and the results are presented in Fig. 7. The PEC reduction of Cr(VI) was easier at a higher applied potential within the range

of 1.0 V–3.0 V. Moreover, the efficiency of electrochemical enhancement ( $E$ , in%) was estimated.

$$E = \left( \frac{k_{\text{PEC}} - k_{\text{PC}}}{k_{\text{PEC}}} \right) \times 100\% \quad (3)$$

According to the above equation [65], the  $E$  value at 1.0 V was calculated to be 45.6%, whereas it increases considerably to 87.0% at 2.0 V. However, the enhancement trend slowed down, with an  $E$  value of 93.6%, when the applied potential further increased to 3.0 V. Thus, 2.0 V was selected for the following study for the purpose of energy conservation.

A large amount of organic pollutants are also observed in Cr(VI)-containing wastewater. For example, EDTA has been detected as a common chelating agent, which may arise from various industrial processes and form metal-EDTA complexes [4–7,66–68]. Thus, in addition to metal ions reduction, the degradation of co-existing organic pollutants was also of vital importance. As illustrated in Fig. 8A and Fig. S10, the simultaneous PEC reduction of Cr(VI) and degradation of EDTA can be observed in the present system. Moreover, the reduction of Cr(VI) was greatly improved by the presence of EDTA. With an increasing EDTA concentration (Fig. 8B), the removal efficiency of Cr(VI) increased from 40% to 91% after 80 min of the PEC reaction. Meanwhile, the presence of other organics was also investigated. As shown in Fig. S11, the presence of either colorless phenol or colored MB dye can greatly promote the reduction of Cr(VI). The organics themselves were also degraded simultaneously. Thus, the  $\text{Fe}_2\text{O}_3\text{-GQDs}/\text{NF-TiO}_2$  composite electrode was suitable for handling Cr(VI)-organic co-polluted wastewater.

Experiments with different initial solution pH were also performed, as pH has always been considered an important factor for Cr(VI) reduction. As shown in Fig. 9A, the reduction of Cr(VI) is easier to carry out under lower pH. The reason may be as follows: (1) The Cr(VI)/Cr(III) redox potential became larger at low pH due to the different predominant states of Cr(VI) ( $E^0(\text{CrO}_4^{2-}/\text{Cr}(\text{OH})_3) = -0.13 \text{ V}$  vs. NHE,  $E^0(\text{HCrO}_4^-/\text{Cr}^{3+}) = 1.35 \text{ V}$  vs. NHE) [69], which led to an increased thermodynamic driving force for Cr(VI) reduction; (2) The VB edge of the photoanode shifted along with the CB edge to a more positive position at lower pH, which led to increased oxidative ability for EDTA degradation [64] and subsequently more efficient electron-hole separation.

In the present study, the PEC experiments were performed using  $\text{Na}_2\text{SO}_4$  as an electrolyte to increase conductivity. Thus, the concentration of  $\text{Na}_2\text{SO}_4$  may also affect the PEC activity for Cr(VI) reduction [70]. As shown in Fig. 9B, the reduction of Cr(VI) was enhanced by increasing the  $\text{Na}_2\text{SO}_4$  concentration. In addition, the enhancement trend slowed down when the  $\text{Na}_2\text{SO}_4$  concentration was further increased to 1.0 M. In general, the above results indicate that the prepared photoanode is suitable for handling high-salinity wastewater.

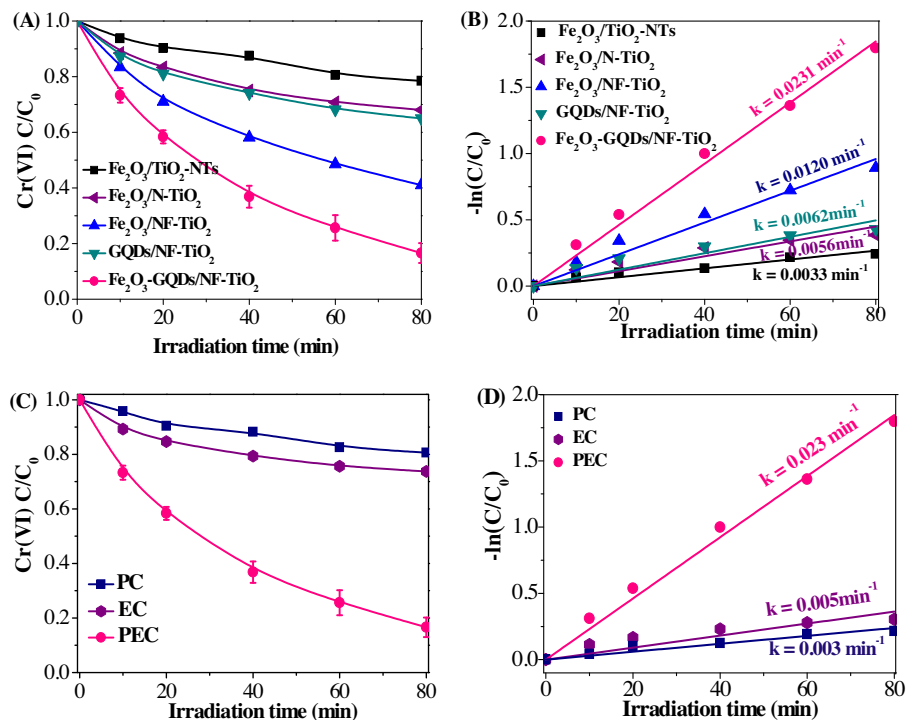


**Fig. 6.** (A) PEC reduction dynamics and (B) pseudo-first-order kinetic curves of Cr(VI) using different photoanodes; (C) Comparison of Cr(VI) reduction dynamics and (D) pseudo-first-order kinetic curves using Fe<sub>2</sub>O<sub>3</sub>-GQDs/NF-TiO<sub>2</sub> electrode under different processes. Reaction conditions: 2.0 V, 0.2 M Na<sub>2</sub>SO<sub>4</sub>, pH 3.0, 80 μM Cr(VI), 1 mM EDTA.

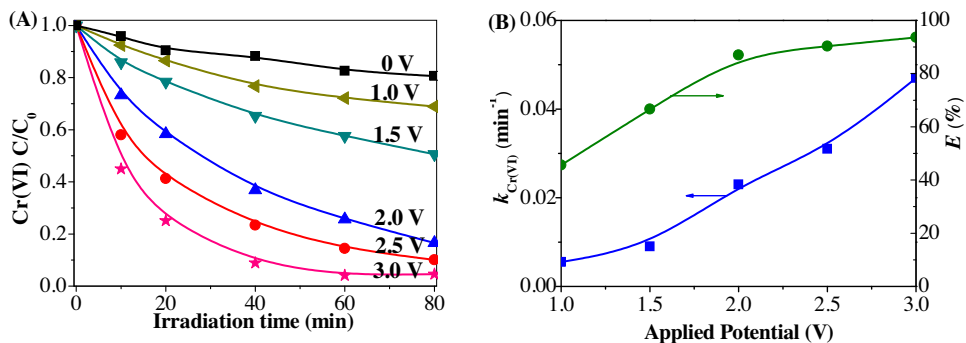


**Fig. 7.** Effect of external potential on the PEC reduction of Cr(VI) on Fe<sub>2</sub>O<sub>3</sub>-GQDs/NF-TiO<sub>2</sub> under visible light irradiation (A) reduction dynamics, (B) estimated rate constants and E%. Reaction conditions: 2.0 V, 0.2 M Na<sub>2</sub>SO<sub>4</sub>, pH 3.0, 80 μM Cr(VI), 1 mM EDTA.

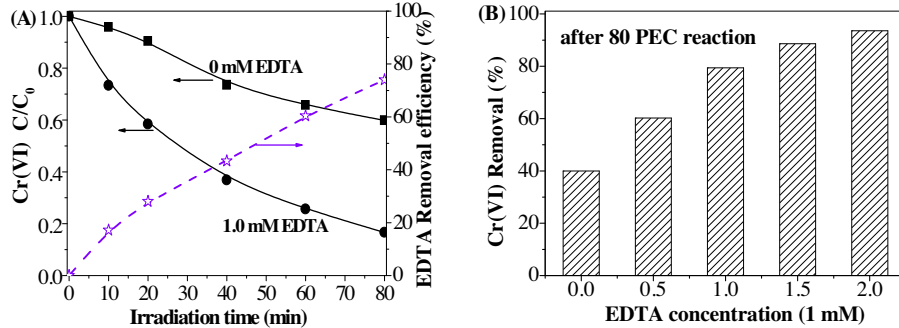


**Fig. 8.** (A) Effect of EDTA concentration on the PEC reduction of Cr(VI) (left) and simultaneous removal efficiency of 1.0 mM EDTA (right) using a Fe<sub>2</sub>O<sub>3</sub>-GQDs/NF-TiO<sub>2</sub> electrode. (B) Relationship between Cr(VI) removal efficiency and coexisting EDTA concentration. External potential: 2.0 V. Electrolyte: 0.2 M Na<sub>2</sub>SO<sub>4</sub>, pH = 3.0.

### 3.6. Stability of the Fe<sub>2</sub>O<sub>3</sub>-GQDs/NF-TiO<sub>2</sub> electrode

As an excellent photocatalytic electrode, the stability of the PEC performance is critical. In the present study, the Fe<sub>2</sub>O<sub>3</sub>-GQDs/NF-

TiO<sub>2</sub> film was evaluated via both a long-time photocurrent test and cyclic PEC experiments for Cr(VI) reduction. As shown in Fig. 10A, the photocurrent generated on the Fe<sub>2</sub>O<sub>3</sub>-GQDs/NF-TiO<sub>2</sub>

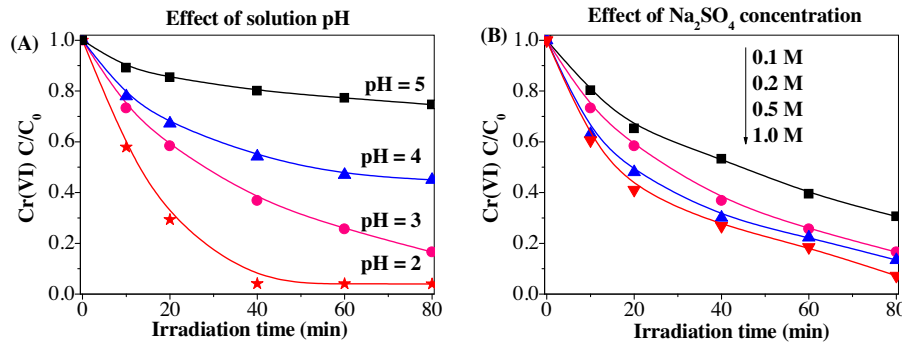


**Fig. 9.** (A) Influence of solution pH and (B) electrolyte concentration on the PEC reduction of Cr(VI). Reaction conditions: Fe<sub>2</sub>O<sub>3</sub>-GQDs/NF-TiO<sub>2</sub>, 80 μM Cr(VI), 1 mM EDTA.

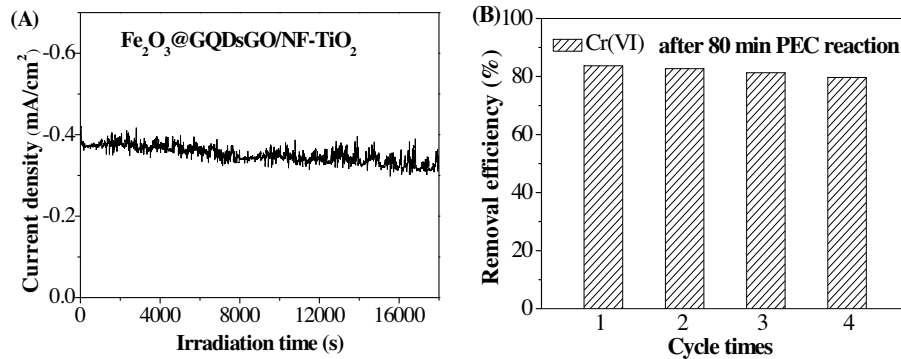


**Fig. 10.** (A) Long-time photocurrent decay curve measured under visible light irradiation at a constant potential of 0.5 V (vs. Ag/AgCl) for Fe<sub>2</sub>O<sub>3</sub>-GQDs/NF-TiO<sub>2</sub> film in 0.1 M Na<sub>2</sub>SO<sub>4</sub> and Na<sub>2</sub>SO<sub>3</sub> mixed aqueous solution; (B) Cyclic removal of both Cr(VI) and phenol using the Fe<sub>2</sub>O<sub>3</sub>-GQDs/NF-TiO<sub>2</sub> photoanode under visible light irradiation.

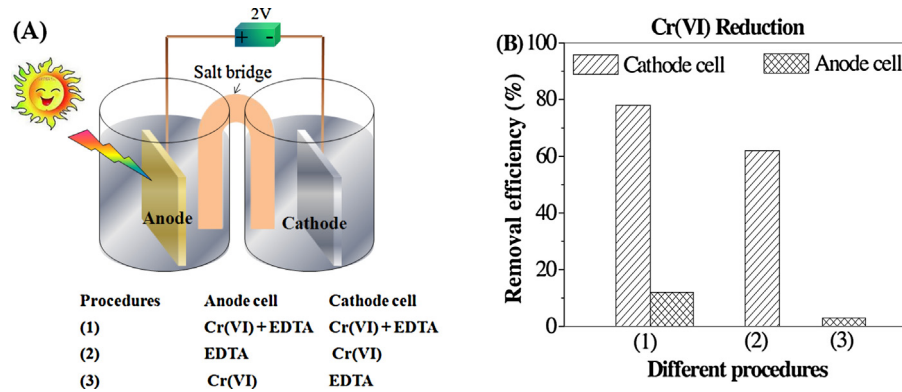


**Fig. 11.** (A) Schematic illustration of experiments using a salt bridge and (B) Cr(VI) removal efficiencies in different PEC processes. Reaction conditions: 2.0 V, 0.2 M Na<sub>2</sub>SO<sub>4</sub>, pH 3.0, 80 μM Cr(VI), 1 mM EDTA.

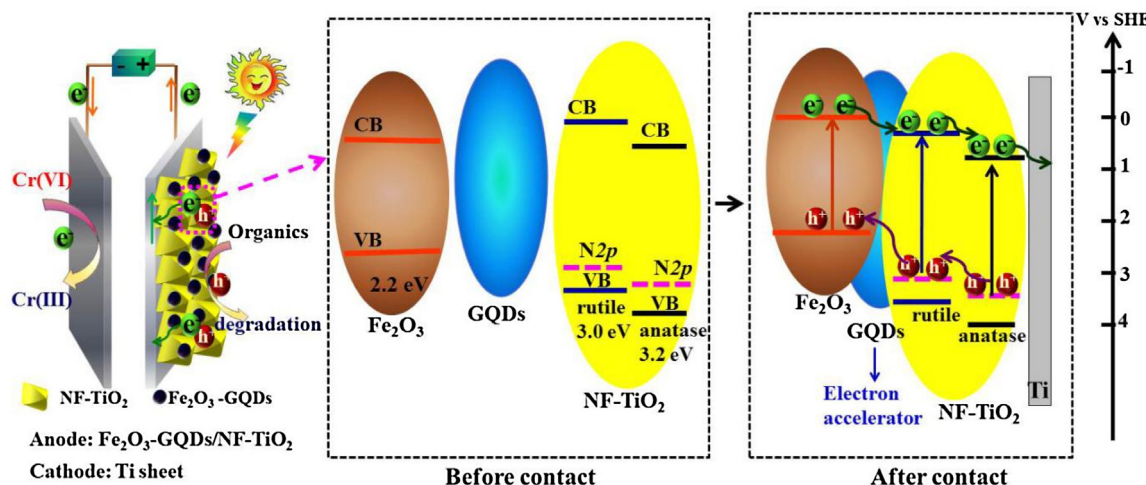
film was extremely stable and exhibited nearly no attenuation within 18,000 s (5 h) of constant visible light irradiation. The optimized film electrode was also tested in 4 successive cyclic PEC runs, and the results are presented in Fig. 10B. The removal efficiencies were relatively consistent over 4 cycles. Overall, the Fe<sub>2</sub>O<sub>3</sub>-GQDs/NF-TiO<sub>2</sub> film electrode exhibited superior PEC performance and stability.

### 3.7. Proposed mechanism

In the present study, the visible-light-active Fe<sub>2</sub>O<sub>3</sub>-GQDs/NF-TiO<sub>2</sub> film was applied as anode with a Ti sheet as cathode, respectively. The photogenerated electrons on the photoanode are anticipated to be driven to the cathode with the assistance of applied positive potential. In this manner, the photogenerated

holes left on the anode and electrons on the cathode will lead to subsequent oxidation and reduction reactions, respectively. Experiments using salt bridges were performed to verify this assumption (Fig. 11A). The PEC reduction of Cr(VI) was performed using two separate glass cells under different conditions, and the results are shown in Fig. 11B. It can be observed that Cr(VI) was predominately reduced in the cathode cell.

Based on all the above results and analyses, tentative mechanisms for the reduction of Cr(VI) and the separation/transfer of photogenerated electron-hole pairs on Fe<sub>2</sub>O<sub>3</sub>-GQDs/NF-TiO<sub>2</sub> are presented in Scheme 2. For NF-TiO<sub>2</sub>, both anatase and rutile phases were identified by XRD analysis. Due to the different band gaps and CB positions [71–73], the intrinsic band difference between anatase and rutile TiO<sub>2</sub> will be beneficial for electron-hole separation. In addition, although α-Fe<sub>2</sub>O<sub>3</sub> was reported to possess a lower inde-



**Scheme 2.** Schematic illustration for the PEC reduction of Cr(VI) (left) and the separation/transfer of photogenerated electron–hole pairs on Fe<sub>2</sub>O<sub>3</sub>-GQDs/NF-TiO<sub>2</sub> during the PEC process (right).

pendent CB position relative to TiO<sub>2</sub>, the same Fermi level tended to be achieved between  $\alpha$ -Fe<sub>2</sub>O<sub>3</sub> and NF-TiO<sub>2</sub> when they were in contact with each other. In this manner, the CB of  $\alpha$ -Fe<sub>2</sub>O<sub>3</sub> would move to a more negative position [29]. XPS analysis (Fig. 3C) has shown that the introduction of GQDs will lead to the dispersion of electron density from the Fe atoms to the GQDs. Herein, the GQDs act as an electron accelerator, which will be beneficial for the process of electron transfer from Fe<sub>2</sub>O<sub>3</sub> to TiO<sub>2</sub>. Finally, the separated electrons will be driven to the cathode by an applied positive potential, and the holes will be kept on the photoanode. Thus, an efficient separation of photogenerated electron–hole pairs will be achieved due to the synergistic effect among Fe<sub>2</sub>O<sub>3</sub>, GQDs and NF-TiO<sub>2</sub>.

#### 4. Conclusion

In the present study, a visible-light active Fe<sub>2</sub>O<sub>3</sub>-GQDs/NF-TiO<sub>2</sub> composite film was fabricated by simultaneously loading  $\alpha$ -Fe<sub>2</sub>O<sub>3</sub> and GQDs onto pyramid-shaped NF-TiO<sub>2</sub>. NH<sub>4</sub>F plays a vital role in transforming tubular TiO<sub>2</sub>-NTs into pyramid-shaped NF-TiO<sub>2</sub> with dominant (101) facets. Easier generation, separation and transfer of e<sup>−</sup>–h<sup>+</sup> pairs was facilitated due to the combined effect of visible-light active components ( $\alpha$ -Fe<sub>2</sub>O<sub>3</sub> and NF-TiO<sub>2</sub>) and excellent electron accelerators (GQDs). For example, electrochemical characterizations indicated that the visible-light-induced photocurrent density at 0.4 V vs. Ag/AgCl was approximately 4 times that on Fe<sub>2</sub>O<sub>3</sub>/TiO<sub>2</sub>-NTs. Superior PEC activity for Cr(VI) reduction and stability were observed when using Fe<sub>2</sub>O<sub>3</sub>-GQDs/NF-TiO<sub>2</sub> as anode with a Ti sheet as cathode. The pseudo first-order rate constant  $k_{Cr(VI)}$  increased by 7 times relative to that on Fe<sub>2</sub>O<sub>3</sub>/TiO<sub>2</sub>-NTs. Furthermore, the selected photoanode also exhibited good stability in the long-time photocurrent test and reuse processes for Cr(VI) reduction. Overall, the present study developed a promising film electrode for environmental application, particularly for treating Cr(VI)-organic co-polluted wastewater.

#### Acknowledgements

This research was supported by Zhejiang Provincial Natural Science Foundation of China (LY14B070002, LY14E080002) and the National Science Foundation of China (21477114, 21103149, 21576237).

#### Appendix A. Supplementary data

Supplementary data associated with this article can be found, in the online version, at <http://dx.doi.org/10.1016/j.apcatb.2016.11.046>.

#### References

- [1] C.C. Chen, W.H. Ma, J.C. Zhao, Chem. Soc. Rev. 39 (2010) 4206–4219.
- [2] Y.Y. Zhu, Y.J. Wang, Q. Ling, Y.F. Zhu, Appl. Catal. B Environ. 200 (2017) 222–229.
- [3] D. Wang, X. Li, J. Chen, X. Tao, Chem. Eng. J. 198–199 (2012) 547–554.
- [4] H. Zeng, S. Liu, B. Chai, D. Cao, Y. Wang, X. Zhao, Environ. Sci. Technol. 50 (2016) 6459–6466.
- [5] X. Zhao, L. Guo, J. Qu, Chem. Eng. J. 239 (2014) 53–59.
- [6] X. Zhao, L. Guo, B. Zhang, H. Liu, J. Qu, Environ. Sci. Technol. 47 (2013) 4480–4488.
- [7] X. Zhao, J. Zhang, J. Qu, Electrochim. Acta 180 (2015) 129–137.
- [8] S.N. Chai, G.H. Zhao, Y.N. Zhang, Y.J. Wang, F.Q. Nong, M.F. Li, D.M. Li, Environ. Sci. Technol. 46 (2012) 10182–10190.
- [9] W.J. Jiang, M. Zhang, J. Wang, Y.F. Liu, Y.F. Zhu, Appl. Catal. B: Environ. 160–161 (2014) 44–50.
- [10] H.B. Fu, L.W. Zhang, S.C. Zhang, Y.F. Zhu, J.C. Zhao, J. Phys. Chem. B 110 (2006) 3061–3065.
- [11] S.M. Zhou, D.K. Ma, P. Cai, W. Chen, S.M. Huang, Mater. Res. Bull. 60 (2014) 64–71.
- [12] R. Asahi, T. Morikawa, T. Ohwaki, K. Aoki, Y. Taga, Science 293 (2001) 269–271.
- [13] M. Mrowetz, W. Balcerzki, A.J. Colussi, M.R. Hoffmann, J. Phys. Chem. B 108 (2004) 17269–17273.
- [14] R. Nakamura, T. Tanaka, Y. Nakato, J. Phys. Chem. B 108 (2004) 10617–10620.
- [15] Q. Wang, C.C. Chen, W.H. Ma, H.Y. Zhu, J.C. Zhao, Chem. Eur. J. 15 (2009) 4765–4769.
- [16] L. Di, H. Hajime, H. Shunichi, O. Naoki, Chem. Mater. 17 (2005) 2596–2602.
- [17] J. Andersen, C. Han, K. O'Shea, D.D. Dionysiou, Appl. Catal. B: Environ. 154–155 (2014) 259–266.
- [18] J. Zhu, S.H. Wang, J.G. Wang, D.Q. Zhang, H.X. Li, Appl. Catal. B: Environ. 102 (2011) 120–125.
- [19] M. Pelaez, N.T. Nolan, S.C. Pillai, M.K. Seery, P. Falaras, A.G. Kontos, P.S.M. Dunlop, J.W.J. Hamilton, J.A. Byrne, K. O'Shea, M.H. Entezari, D.D. Dionysiou, Appl. Catal. B: Environ. 125 (2012) 331–349.
- [20] Y. Wang, Y. Zhang, G.H. Zhao, H. Tian, H. Shi, T. Zhou, ACS Appl. Mater. Interfaces 4 (2012) 3965–3972.
- [21] M. Forster, R.J. Potter, Y. Ling, Y. Yang, D.R. Klug, Y. Lid, A.J. Cowan, Chem. Sci. 6 (2015) 4009–4016.
- [22] D. Xiao, K. Dai, Y. Qu, Y. Yin, H. Chen, Appl. Surf. Sci. 358 (2015) 181–187.
- [23] P. Cai, S.M. Zhou, D.K. Ma, S.N. Liu, W. Chen, S.M. Huang, Nano-Micro Lett. 7 (2015) 183–193.
- [24] W. Hung, T. Chien, C. Tseng, J. Phys. Chem. C 118 (2014) 12676–12681.
- [25] X. Li, H. Lin, X. Chen, H. Niu, J. Liu, T. Zhang, F. Qu, Phys. Chem. Chem. Phys. 18 (2016) 9176–9185.
- [26] J. Liu, S. Yang, W. Wu, Q. Tian, S. Cui, Z. Dai, F. Ren, X. Xiao, C. Jiang, ACS Sustain. Chem. Eng. 3 (2015) 2975–2984.
- [27] Y.Q. Cong, Z. Li, Y. Zhang, Q. Wang, Q. Xu, Chem. Eng. J. 191 (2012) 356–363.
- [28] S.Y. Kuang, L.X. Yang, S.L. Luo, Q.Y. Cai, Appl. Surf. Sci. 255 (2009) 7385–7388.
- [29] P. Luan, M. Xie, D. Liu, X. Fu, L. Jing, Sci. Rep. 4 (2014) 6180.
- [30] N. Gao, X. Fang, Chem. Rev. 115 (2015) 8294–8343.

[31] X.J. Bai, L. Wang, Y.J. Wang, W.Q. Yao, Y.F. Zhu, *Appl. Catal. B: Environ.* 152–153 (2014) 262–270.

[32] Y.B. Wang, H.Y. Zhao, G.H. Zhao, *Appl. Catal. B: Environ.* 164 (2015) 396–406.

[33] H.Y. Zhao, Y.J. Wang, Y.B. Wang, T.C. Cao, G.H. Zhao, *Appl. Catal. B: Environ.* 125 (2012) 120–127.

[34] Y.J. Wang, G.H. Zhao, S.N. Chai, H.Y. Zhao, Y.B. Wang, *ACS Appl. Mater. Inter.* 5 (2013) 842–852.

[35] Y.N. Zhang, H.Y. Tian, G.H. Zhao, *ChemElectroChem* 2 (2015) 1728–1734.

[36] Y.Q. Zhang, D.K. Ma, Y.G. Zhang, W. Chen, S.M. Huang, *Nano Energy* 2 (2013) 545–552.

[37] Y.W. Zeng, D.K. Ma, W. Wang, J.J. Chen, L. Zhou, Y.Z. Zheng, K. Yu, S.M. Huang, *Appl. Surf. Sci.* 342 (2015) 136–143.

[38] Y.Q. Zhang, D.K. Ma, Y. Zhuang, X. Zhang, W. Chen, L.L. Hong, Q.X. Yan, K. Yu, S.M. Huang, *J. Mate. Chem.* 22 (2012) 16714–16718.

[39] Z. Xiong, X.S. Zhao, *J. Am. Chem. Soc.* 134 (2012) 5754–5757.

[40] T.R. Gordon, M. Cargnello, T. Paik, F. Mangolini, R.T. Weber, P. Fornasiero, C.B. Murray, *J. Am. Chem. Soc.* 134 (2012) 6751–6761.

[41] J. Pan, G. Liu, G.Q. Lu, H. Cheng, *Angew. Chem. Int. Ed.* 123 (2011) 2181–2185.

[42] T. Tachikawa, S. Yamashita, T. Majima, *J. Am. Chem. Soc.* 133 (2011) 7197–7204.

[43] Y.Q. Cong, Z. Li, Q. Wang, Y. Zhang, Q. Xu, F.X. Fu, *Acta Phys. Chim. Sin.* 28 (2012) 1489–1496.

[44] Q. Wang, X. Chen, K. Yu, Y. Zhang, Y. Cong, *J. Hazard. Mater.* 246–247 (2013) 135–144.

[45] A. Idris, N. Hassan, R. Rashid, A.F. Ngomsik, *J. Hazard. Mater.* 186 (2011) 629–635.

[46] J. Ge, M. Lan, B. Zhou, W. Liu, L. Guo, H. Wang, Q. Jia, G. Niu, X. Huang, H. Zhou, X. Meng, P. Wang, C.S. Lee, W. Zhang, X. Han, *Nat. Comm.* 5 (2014) 4596.

[47] Y. Dong, H. Pang, H. Yang, C. Guo, J. Shao, Y. Chi, C. Li, T. Yu, *Angew. Chem. Int. Ed.* 52 (2013) 7800–7804.

[48] S. Chen, Y. Xin, Y. Zhou, F. Zhang, Y. Ma, H. Zhou, L. Qi, *J. Mater. Chem. A* 3 (2015) 13377–13383.

[49] X. Lv, X. Xue, G. Jiang, D. Wu, T. Sheng, H. Zhou, X. Xu, *J. Colloid Interf. Sci.* 417 (2014) 51–59.

[50] X. Yu, Y. Zhang, X. Cheng, *Electrochim. Acta* 137 (2014) 668–675.

[51] K. Parvez, Z. Wu, R. Li, X. Liu, R. Graf, X. Feng, K. Müllen, *J. Am. Chem. Soc.* 136 (2014) 6083–6091.

[52] R. Liu, D. Wu, X. Feng, K. Müllen, *J. Am. Chem. Soc.* 133 (2011) 15221–15223.

[53] G. Liu, H. Yang, X. Wang, L. Cheng, J. Pan, G. Lu, H. Cheng, *J. Am. Chem. Soc.* 131 (2009) 12868–12869.

[54] J. Pan, G. Liu, G.Q. Lu, H. Cheng, *Angew. Chem. Int. Ed.* 123 (2011) 2181–2185.

[55] Y. Li, Y. Hu, Y. Zhao, G. Shi, L. Deng, Y. Hou, L. Qu, *Adv. Mater.* 23 (2011) 776–780.

[56] Y.Q. Cong, M.M. Chen, T. Xu, Y. Zhang, Q. Wang, *Appl. Catal. B: Environ.* 147 (2014) 733–740.

[57] A. Kleiman-Shwarzstein, A.J.F.Y.-S. Hu, G.D. Stucky, E.W. McFarland, *J. Phys. Chem. C* 112 (2008) 15900–15907.

[58] M. Sathish, B. Viswanathan, R.P. Viswanath, C.S. Gopinath, *Chem. Mater.* 17 (2005) 6349–6353.

[59] H.J. Shi, G.H. Zhao, *J. Phys. Chem. C* 118 (2014) 25939–25946.

[60] N. Mirbagheri, D. Wang, C. Peng, J. Wang, Q. Huang, C. Fan, E.E. Ferapontova, *ACS Catal.* 4 (2014) 2006–2015.

[61] A.J. Bard, L.R. Faulkner, John Wiley & Sons, New York, 2001, pp. 386.

[62] H. Chen, G. Liu, L. Wang, *Sci. Rep.* 5 (2015) 10852.

[63] Y. Li, W.Q. Cui, L. Liu, R.L. Zong, W. Yao, Y.H. Liang, Y.F. Zhu, *Appl. Catal. B: Environ.* 199 (2016) 412–423.

[64] Q. Wang, X.D. Shi, E.Q. Liu, J.J. Xu, J.C. Crittenden, Y. Zhang, Y.Q. Cong, *Ind. Eng. Chem. Res.* 55 (2016) 4897–4904.

[65] S. Garcia-Segura, S. Dosta, J.M. Guilemany, E. Brillas, *Appl. Catal. B: Environ.* 132–133 (2013) 142–150.

[66] G. Kim, W. Choi, *Appl. Catal. B: Environ.* 100 (2010) 77–83.

[67] X. Zhao, L. Guo, C. Hu, H. Liu, J. Qu, *Appl. Catal. B: Environ.* 144 (2014) 478–485.

[68] H. Zeng, S. Tian, H. Liu, B. Chai, X. Zhao, *Chem. Eng. J.* 301 (2016) 371–379.

[69] Q. Wang, X.D. Shi, E.Q. Liu, J.C. Crittenden, X.J. Ma, Y. Zhang, Y.Q. Cong, *J. Hazard. Mater.* 317 (2016) 8–16.

[70] J. Chen, Y. Xia, Q. Dai, *Electrochim. Acta* 165 (2015) 277–287.

[71] Y. Nosaka, A.Y. Nosaka, *J. Phys. Chem. Lett.* 7 (2016) 431–434.

[72] M.G. Ju, G. Sun, J. Wang, Q. Meng, W.Z. Liang, *ACS Appl. Mater. Inter.* 6 (2014) 12885–12892.

[73] P. Deaík, B. Aradi, T. Frauenheim, *J. Phys. Chem. C* 115 (2011) 344–346.